Numerical simulation and prediction of dilution during laser deposition

Zhiqiang Fan[1], Anand Jambunathan[2], Todd E. Sparks[1], Jianzhong Ruan[1], Yu Yang[1], Yaxin Bao[1] and Frank Liou[1]

[1]Department of Mechanical and Aerospace Engineering, University Of Missouri–Rolla

[2] Department of Metallurgical Engineering, University Of Missouri–Rolla

1870 Miner Circle, Rolla, MO 65409

573-341-4603, liou@umr.edu

ABSTRACT

The laser additive manufacturing technique of laser deposition allows quick fabrication of fully-dense metallic components directly from Computer Aided Design (CAD) solid models. The applications of laser deposition include rapid prototyping, rapid tooling and part refurbishment. The development of an accurate predictive model for laser deposition is extremely complicated due to the multitude of process parameters and materials properties involved. In this work, a heat transfer and fluid flow model is developed. The model is used to predict dilution under varying process parameters for deposits of Ti-6Al-4V. Experimental validation of the predicted dilution is presented. The laser used is a direct diode laser.

1. INTRODUCTION

Laser deposition is an extension of the laser cladding process for rapid prototyping of fully dense metal components. This laser additive manufacturing technique allows quick fabrication of fully-dense metallic components directly from Computer Aided Design (CAD) solid models. The applications of laser deposition include rapid prototyping, rapid tooling and part refurbishment. A primary objective of the laser deposition process is to achieve porosity free added layers with good bonding to the substrate and with low dilution of the added layer in the substrate. Thus, dilution is among the major concerns for the laser deposition process. Dilution is an important parameter for the laser deposition process because it indexes the bonding between the added layer and the substrate, and the utilization efficiency for the laser power. High dilution indicates that too much laser power has been used to re-melt the substrate and overheating may occur while no dilution at all leads to poor bonding to the substrate and even lack of fusion. Many investigations have been done on substrate dilution during the past years [1-11]. It is considered that the control of laser deposition for a given level of dilution which is sufficient to establish metallurgical bonding but which minimizes dilution would be desirable. However, such control is difficult because dilution highly depends on the metallurgical properties of the materials applied and the varying process parameters.

The authors have developed a self-consistent heat transfer and fluid flow model to predict dilution under different process parameters during laser deposition. In this study, A coaxial diode laser deposition system, LAMP (developed at UMR), is considered for simulations and experiments. The blown powder method is used to deliver power. As the primary laser in the

LAMP system, diode laser is believed to have a number of process advantages as opposed to the CO_2 or Nd:YAG laser, including the better material coupling efficiency (laser absorption) and better beam profile for laser deposition. The beam profile of a diode laser is generally uniform due to the nature of the beam formation process. This profile is beneficial for many applications where uniform heating of a surface is required, as in laser surface hardening, laser alloying and laser cladding [13]. Material of both powder and substrates is Ti-6Al-4V alloy, which is widely used in the aerospace industry and especially suitable for laser processing, since Ti-6Al-4V is still classified as one of the extremely difficult-to-machine materials using conventional machining [14].

2. MATHEMATICAL MODEL

2.1 Governing Equations

2.1.1 Momentum and energy conservation

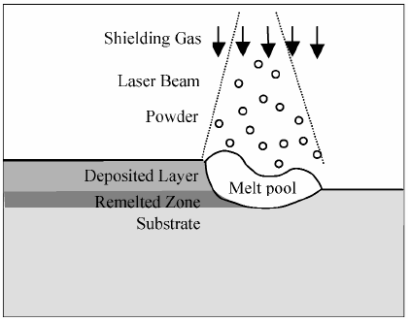

Fig.1-Schematic of the laser deposition system

Figure 1 shows a schematic diagram of the laser deposition system. In the laser deposition process, melting and solidification cause the phase transformation at the solid/liquid interface. A mushy zone containing solid and liquid is formed. To track the solid/liquid interface evolution, in this study the continuum model developed by Bennon and Incropera [15, 16] is adopted, which is an extension of the classical mixture theory. The momentum equations are written for the mixture velocities, relying on the value of the permeability in each control volume to determine whether flow through porous mush is important in that control volume.

For the system of interest, a Newtonian, incompressible, laminar flow is assumed in the melt pool.

The conservation equations for mass, momentum and energy are summarized as follows:

Continuity

$$\frac{\partial \rho}{\partial t} + \nabla \cdot (\rho \vec{V}) = 0 \tag{1}$$

Momentum

$$\frac{\partial}{\partial t}(\rho u) + \nabla \cdot (\rho \vec{V} u) = \nabla \cdot (\mu_l \frac{\rho}{\rho_l} \nabla u) - \frac{\partial p}{\partial x} - \frac{\mu_l}{K} \frac{\rho}{\rho_l}(u - u_s) + S_{\phi x} \tag{2}$$

$$\frac{\partial}{\partial t}(\rho v) + \nabla \cdot (\rho \vec{V} v) = \nabla \cdot (\mu_l \frac{\rho}{\rho_l} \nabla v) - \frac{\partial p}{\partial y} - \frac{\mu_l}{K} \frac{\rho}{\rho_l}(v - v_s) + \rho g + S_{\phi y} \tag{3}$$

Energy

$$\frac{\partial(\rho h)}{\partial t} + \nabla \cdot (\rho \vec{V} h) = \nabla \cdot (k \nabla T) - \nabla \cdot (\rho (h_l - h)(\vec{V} - \vec{V}_s) \quad (4)$$

In equations (1)-(4), the continuum density, specific heat, thermal conductivity, vector velocity, and enthalpy are defined as follows:

$$\rho = g_s \rho_s + g_l \rho_l \qquad c = f_s c_s + f_l c_l \qquad k = g_s k_s + g_l k_l$$

$$\vec{V} = f_s \vec{V}_s + f_l \vec{V}_l \qquad h = f_s h_s + f_l h_l \quad (5)$$

The volume fractions of liquid can be obtained from Swaminathan and Voller's general enthalpy method [17], although other relationships are possible [18]. Swaminathan and Voller summarized four possible enthalpy-temperature curves with different liquid fraction temperature relationships. In this work, both the deposit and the substrate materials are Ti-6Al-4V, for which Curve B is more appropriate where there is a linear evolution of the latent heat over the solidification range $T_l - T_s$. The liquid fraction temperature relationship for this type of enthalpy-temperature curve is given by:

$$g_l = \begin{cases} 0 & \text{if } T < T_s \\ \dfrac{T - T_s}{T_l - T_s} & \text{if } T_s \le T \le T_l \\ 1 & \text{if } T > T_l \end{cases} \quad (6)$$

The other volume and mass fractions are can be obtained by:

$$f_l = \frac{g_l \rho_l}{\rho} \qquad f_s = \frac{g_s \rho_s}{\rho} \qquad g_s + g_l = 1 \qquad f_s = 1 - f_l \quad (7)$$

The phase enthalpy for the solid and the liquid can be expressed as:

$$h_s = \int_0^T c_s(T) dT \qquad h_l = \int_0^{T_s} c_s(T) dT + \int_{T_s}^T c_l(T) dT + L_m \quad (8)$$

where L_m is the latent heat of melting.

The assumption of a multiphase region permeability requires consideration of growth morphology specific to the alloy under consideration. The present study follows the approach suggested by Bennon and Incropera [15, 16], permeability, K, is assumed to vary with liquid volume fraction according to the Kozeny-Carman equation[19] derived from Darcy's law:

$$K = K_0 \frac{g_l^3}{(1 - g_l)^2} \quad (9)$$

where K_0 is a constant depending on the morphology and size of the dendrites in the mushy zone.

The $S_{\phi x}$ and $S_{\phi y}$ in the momentum equations are source terms contributed by the interfacial forces such as thermocapillary force and surface tension.

2.1.2 Tracking of the Free Surface

The liquid/vapor interface, or the free surface of the melt pool, is very complex due to surface tension, thermocapillary force, and impaction of the powder injection. In this study, the Volume-Of-Fluid (VOF) method is employed to track the evolution of the moving free surface of the melt pool. The melt pool configuration is defined in terms of a volume of fluid function, F(x,y,t), which represents the volume of fluid per unit volume and satisfies the conservation equation:

$$\frac{\partial F}{\partial t} + (V \cdot \nabla)F = 0 \tag{10}$$

2.2 Boundary Conditions

2.2.1 Top Liquid-Vapor Free Surface

(1) Momentum balance

A free surface cell is subject to the following normal and tangential boundary condition:
Tangential stress balance:

$$\mu(\frac{\partial u_s}{\partial n} + \frac{\partial v_n}{\partial s}) = \frac{\partial \gamma}{\partial T} \cdot \frac{\partial T}{\partial s} \tag{11}$$

Normal stress balance:

$$p = p_v + \gamma \cdot \kappa \tag{12}$$

where u_s and v_s are the tangential and normal velocity component at the free surface. p_v is the vapor pressure in the gas region. γ and κ represent surface tension coefficient and curvature, respectively. κ is given in [18]:

$$\kappa = -(\nabla \cdot \vec{n}) = \frac{1}{|\vec{n}|}\left[(\frac{n}{|\vec{n}|} \cdot \nabla)|\vec{n}| - (\nabla \cdot \vec{n}) \right] \tag{13}$$

where $\vec{n}$ is a normal vector of local free surface, which is a gradient of VOF function:

$$\vec{n} = \nabla F \tag{14}$$

(2) Energy balance

Energy balance at the free surface satisfies the following equation:

$$k\frac{\partial T}{\partial n} = \frac{\eta(P_{laser} - P_{atten})}{\pi R^2} - h_c(T - T_\infty) - \varepsilon\sigma(T^4 - T_\infty^4) - \dot{m}_e L_v \tag{15}$$

where terms on the right-hand side are laser irradiation, convective heat loss, radiation heat loss and evaporation heat loss, respectively. P_{laser} is the power of laser beam, P_{atten} is the power

attenuated by the powder cloud, R is the laser beam radius, η is the laser absorption coefficient, which is measured by Sparks et al. [20]. The laser energy distribution is assumed to be uniform, which is close to the actual conditions. P_{atten} is calculated according to Frenk et al's model [21] with minor modification:

$$P_{atten} = P_{laser}\left[1 - \exp\left(-\frac{3Q_{ext}\dot{m}l}{\pi\rho r_p D_{jet} v_p}\right)\right] \tag{16}$$

where $\dot{m}$ denotes the powder mass flow rate, l is the stand-off distance from the nozzle exit to the substrate, ρ is powder density, r_p is the radius of the powder particle, D_{jet} is the diameter of the powder jet, v_p is the powder injection velocity, and Q_{ext} is the extinction coefficient. It is assumed that the extinction cross section is close to the actual geometrical cross section, and Q_{ext} takes a value of unity.

In the evaporation term, $\dot{m}_e$ is the evaporation mass flux and L_v is the latent heat of evaporation. According to Choi et al.'s "overall evaporation model" [22], $\dot{m}_e$ is of the form:

$$\log \dot{m}_e = A + 6.1210 - \frac{18836}{T} - 0.5\log T \tag{17}$$

where A is a constant dependent on the material.

(3) Mass Balance

Powder particles that inject onto the top surface can be classified into three categories. (1) Those powder particles that have not been melted during their passage and hit the solid part of the substrate will deflect and lose. (2) Those powder particles that have been melted before they arrive on the substrate and impact the solid part of the substrate will stick to the surface of the substrate. (3) Those powder particles that fall into the melt pool including melted and unmelted will merge and mix with the molten liquid in the melt pool [23]. In this study, the powder particles belonging to the last two cases will be utilized .

The mass ratio of utilized powder to total powder is related to many factors, including melt pool dimensions and geometry, temperatures of the melt pool surface and the solid part of the substrate near the melt pool, the stand off distance between the substrate top surface and the end of the nozzle, and powder concentration distribution. Since the former two factors can be simulated in the present work, and the third factor is known for a specific experiment, the last factor needs to be modeled or measured by experiments. In this study, Pinkerton and Li's model [24] is applied. In their model, two distinct functions are applied to describe the powder concentration distribution along the central axis before and after the merge point, respectively. This model is for coaxial deposition nozzle.

2.2.2 Bottom and side wall surfaces

The boundary conditions at the bottom, left and right wall satisfy the following equations:

$$k\frac{\partial T}{\partial n} = -h_c(T - T_\infty) \tag{18}$$

$$u = 0 \qquad v = 0 \tag{19}$$

Note that the radiation heat loss at these surfaces is neglected due to the fact that the temperature differences at these surfaces are not large.

2.2.3 Heating of powder particles

Powder particles are heated by the laser beam during their flight, and accumulated energy is finally transmitted to the substrate. In this study, a model proposed by Jouvard et al., [25] which is in good agreement with the experiment, is taken in the calculation of the powder temperature.

2.3 Numerical Solution

The SOLA-VOF algorithm [26] is used to solve the continuity and momentum equation (2)-(4). At each time step, the discretized momentum equations calculate new velocities in terms of an estimated pressure field. Then the pressure field is iteratively adjusted and velocity changes induced by each pressure correction are added to the previous velocities. This iterative process is repeated until the continuity equation is satisfied under an imposed tolerance by the newly computed velocities [27]. The energy equation (4) is solved by an implicit method. Staggered grids are employed where the temperatures and pressures are located at the cell center and the velocities at the walls. Uniform grid points were utilized with the mesh size of 10μm, which was proved to achieve grid independence. The time step is taken at the level of 10^{-6}s initially and adapted subsequently according to the convergence and stability requirements of SOLA-VOF.

3. Simulation Results

The parameters for the simulation are chosen based on the capability of our experimental facilities to compare the simulation results with the experimental measurements. A continuous wave diode laser with an 808 nm wavelength is considered as the energy source. The laser intensity distribution is uniform. Three laser powers of 490,700, and 910W, three travel speed of 15, 20, and 25ipm, and three powder mass flow rate of 4, 6, 8g/min are considered. For substrates, Ti-6Al-V4 plates with a thickness of 0.25 inch are selected. Ti-6Al-V4 powder particles with a diameter from 40 to 140 μm are considered as deposit material. The laser absorption coefficient is measured by Sparks et al. [20]. Powder injection speed of 0.1–0.9 m/s

is obtained using Pan's stochastic non-spherical particle collision model [28].
Fig. 1 shows the simulation results at t = 250 ms for one case in which laser power is 700W, travel speed is 20ipm, and powder mass flow rate is 8g/min. As expected, the melt pool depth in this case is small, that is, the melt pool is 'flat' since the laser power distribution is uniform instead of Gaussian.

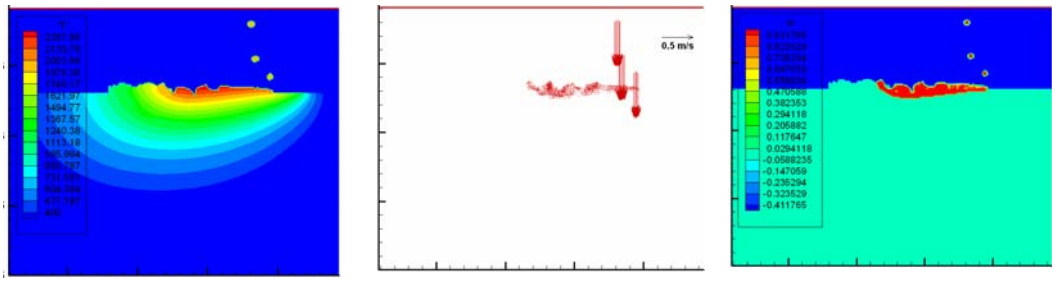

(a) Temperature field (b) Velocity field (c) Volume of Fluid

Figure 1–Simulation results at t = 130 ms for the case: laser power: 910W, travel speed: 20ipm, powder mass flow rate: 4.68g/min.

It is convenient to compute dilution using the function of Volume of Fluid (VOF), which help visualize the melt pool clearly. A cell with a VOF value greater or equal to 0.5 is counted as a liquid cell. Dilution η_d is defined as the ratio of molten bulk material of cross section A_b to the total molten cross section $A_c + A_b$ [32]:

$$\eta_d = \frac{A_b}{A_b + A_c} \tag{20}$$

Fig.2 shows how the melt pool evolves. Fig. 2 (a)-(c) shows the process in which a complete melt pool forms. Fig. 2 (d)-(f) shows that the melt pool is entering a "steady state" in terms of shape and dimensions. The dilution calculation is based on the average value of the transient data in a "steady state" of the melt pool. The simulation results of dilution for different cases are presented in the next section.

4. Experimental results and model validation

4.1 Experimental Setup

The experiments were performed on the LAMP system shown in Fig. 3. The system consists of a diode laser, powder delivery unit, 5-axis CNC machine, and monitoring subsystem. The laser system used in the study was Nuvonyx (Nuvonyx Inc.) ISL-1000M Laser Diode System which combines state-of-the-art micro-optics with laser diodes to produce the only single wavelength fiber coupled direct diode laser at power levels up to 1000 watts CW. The laser emits at 808 nm and operates in the continuous wave (CW) mode. To protect oxidization of Ti-6Al-V4, the system is covered in an environmental chamber to supply argon gas for titanium deposition. The laser spot diameter is 2.5 mm. For the other aspects of the system architecture, refer to Liou et al. [33] and Boddu et al.[34].

Ti-6A1-4V powder (Accumet Materials Co.) has diameters between 40 μm and 140 μm. The substrates have dimensions of 2.5×2.5×0.4 in.

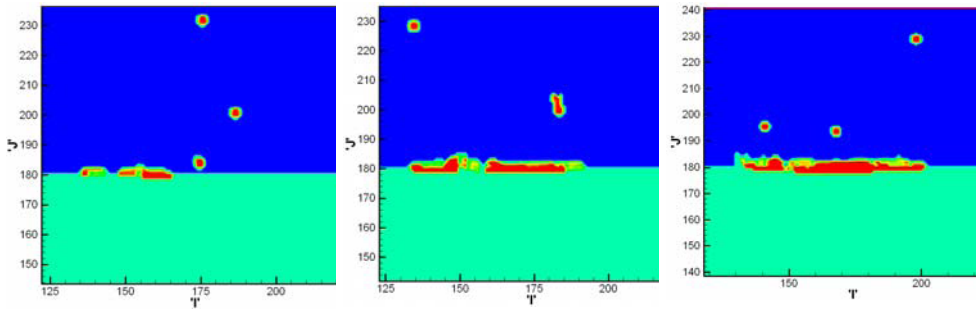

(a) t = 50 ms (b) t = 60 ms (c) t = 70 ms

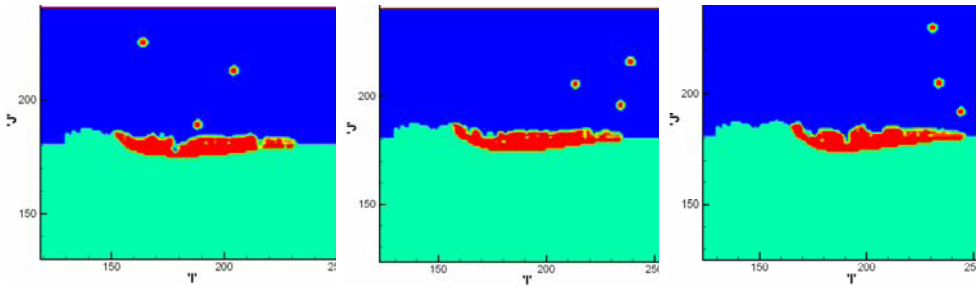

(d) t = 110 ms (e) t = 120 ms (f) t = 130 ms

Figure 2–Evolution of melt pool for the case: laser power: 910W, travel speed: 20ipm, and powder mass flow rate: 4.68g/min

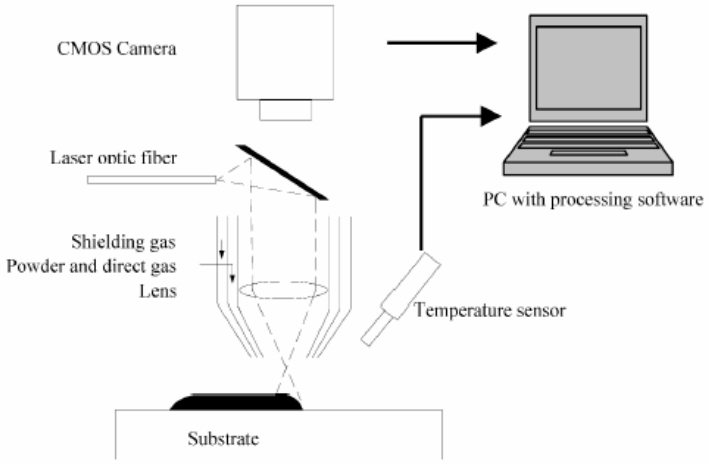

Figure 3-Schematic of experimental setup

4.2 Experimental Procedure

The Ti-6Al-4V samples were irradiated using a laser beam with a beam spot diameter of 2.5 mm and laser powers (measured using a power meter) of 490-910W. The laser deposited samples were cut using a Wire-EDM machine. A SEM (Scanning Electron Microscope) line trace was used on each of the samples to determine the dilution of the clad layer. The deposited Ti-6Al-4V is of Widmansttaten structure. The substrate has a rolled equi-axed alpha+ beta structure. Even though these two structures are considerably different and are easily distinguishable, the HAZ is large and has a martensitic structure that can be associated with it. Hence small quantity of tool steel in the order of 5% was mixed with Ti-6Al-4V. The small quantity makes sure that it does not drastically change the deposit features of a 100 % Ti-6Al-4V deposit. At the same time, the presence of Cr in tool steel makes it easily identifiable by means of EDS scans using SEM. Knowing the exact location of Cr in the substrate would provide the depth of the melt pool in the substrate to measure dilution.

4.3 Results

A dilution analysis using SEM is shown in Fig.4. The upper part is the deposit. The lower part is the re-melt area, only part of it is shown in the images. In order to understand the effects of laser power, travel speed and powder mass flow rate on dilution, and to validate the numerical simulation, both simulation results and experimental results are shown in Fig. 5-7.

Table 2 Measured and simulated dilution on Ti-6Al-4V

Laser Power (W)	Travel Speed (in./min)	Powder Mass Flow Rate (g/min)	Dilution Depth (μm)		Dilution (%)	
			Measured	Simulated	Measured	Simulated
700	15	4.68	108	80	18.7	15.3
	20	4.68	77	60	15.8	13.2
	25	4.68	51	40	12.3	10.4
	20	5.7	61	50	13.1	11.0
	20	6.7	56	50	11.8	10.7
770	20	4.68	105	90	18.5	17.0
840	20	4.68	137	110	21.5	18.4
910	15	4.68	225	170	26.1	22.2
	20	4.68	158	130	22.3	19.5
	25	4.68	133	110	20.2	18.7
	20	5.7	109	100	17.6	16.3
	20	6.7	101	90	16.8	15.4

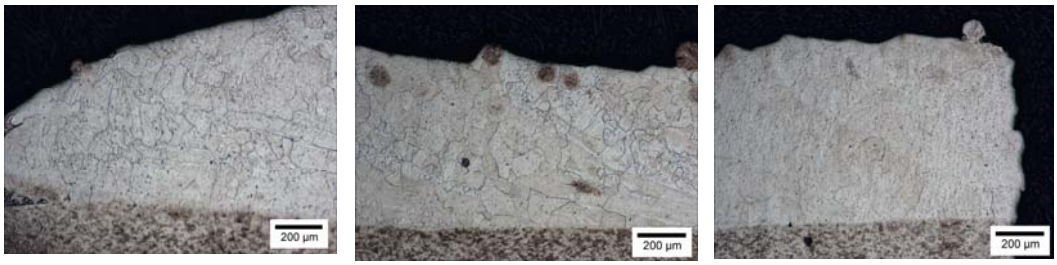

(a) Beginning of deposit (b) Middle of deposit (c) End of deposit

Figure 4-SEM pictures of dilution analysis. (Laser power: 910W, travel speed: 20ipm, powder mass flow rate: 6.7g/min)

5. Discussion

Dilution depth depends on the energy absorbed by the substrate, given the specific material, the geometry of the substrate, laser beam spot size, and the beam profile. Laser power and laser travel speed determine the total energy density potentially absorbed by the substrate. Powder mass flow rate affects the energy actually absorbed by the substrate by the mechanism of power attenuation due to the powder cloud. Laser power, travel speed and powder mass flow rate are the three main process parameters to determine the dilution depth.

Dilution, defined as the ratio of the cross section of the molten substrate material to the total molten cross section, depends on both the dilution depth and the cross section area of the clad. The cross section area of the clad is determined by the clad height and the ripple of clad surface, which are out of this paper's scope.

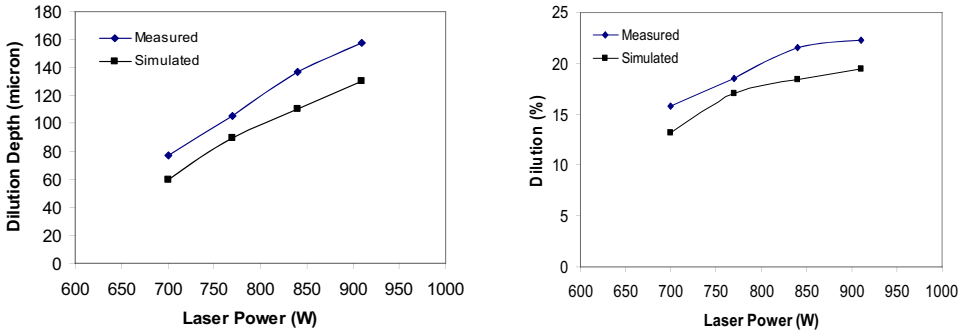

(a) Dilution depth (b) Dilution

Figure 5-Dilution depth and dilution as a function of laser power for travel speed of 20 ipm and powder mass flow rate of 4.68g/min for laser deposited Ti-6Al-4V

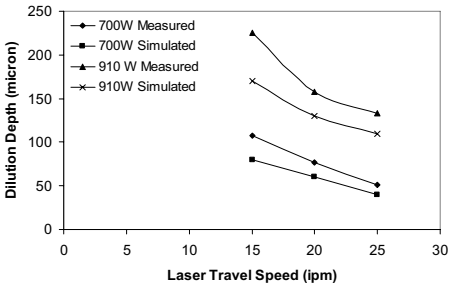

(a) Dilution depth

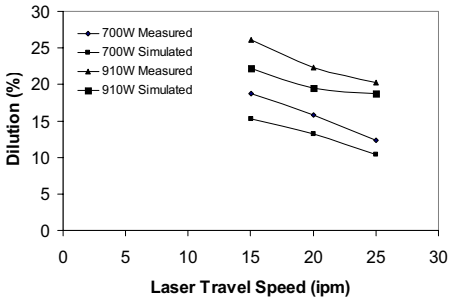

(b) Dilution

Figure 6-Dilution depth and dilution as a function of laser travel speed for powder mass flow rate of 4.68g/min for laser deposited Ti-6Al-4V

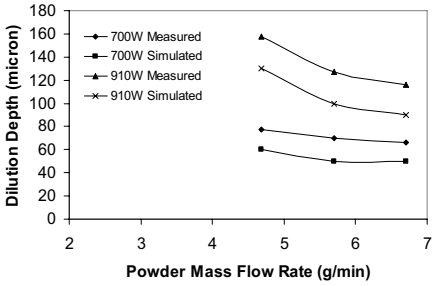

(a) Dilution depth

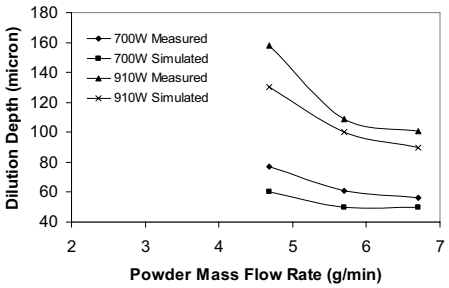

(b) Dilution

Figure 7-Dilution depth and dilution as a function of powder mass flow rate for travel speed of 20 ipm for laser deposited Ti-6Al-4V

From Fig. 5-6, it can be seen that an increase in the laser power will increase the dilution depth. An increase in the laser travel speed will decrease the dilution depth. It is clear that the dilution depth has a linear dependence on the laser power and the laser travel speed. This is easy to understand. As the laser power increases, more power is available for melting the substrate. As travel speed decreases, the laser material interaction time is extended. But since the powder catchment efficiency and thus the cross section area of the clad also increase with increased laser power and decreased laser travel speed the dilution can be seen not to vary proportionally with the dilution depth.

From Fig. 7, it can be seen that an increase in powder mass flow rate will decrease the dilution depth. But the effect of powder mass flow rate on dilution depth is more significant at a lower level of powder mass flow. It is likely that at a lower level of powder mass flow, the effect of powder mass flow rate on powder catchment efficiency is more significant. Also at a higher level of laser power, the effect of powder mass flow rate on dilution depth is more significant. It is likely that at a higher level of laser power, on one hand more power is attenuated given a constant attenuation ratio and more power is absorbed by the powder; on the other hand, the deposited material can decrease the temperature gradients more significantly.

From Fig. 5-7, we can see that the general trend between simulations and experiments is

consistent. The errors between the simulated and measured dilution depths are analyzed to come from four aspects: (1) Resolution of the computational mesh (that is, the mesh size) limits the accuracy of the simulation. In this study, mesh size is 10 μm. But the resolution of SEM measurement is 1 μm. (2) The SEM measurement of the dilution depth may bring about some errors. This method described before may not be very accurate since it is to track the trend of Chromium distribution. (3) The model is two-dimensional but the process is three dimensional in nature. The model intrinsically neglects heat and mass transfer in the third dimension. One can see that the errors between the simulated and measured dilution depths increase with increase laser power and decreased laser travel speed. This may be because that at a higher energy density heat and mass transfer in the third dimension is more significant. (4) The uncertainties of the material properties and the appropriateness of the sub-models are other possible sources of the errors.

In this study, the model is validated in terms of dilution depth and dilution. This heat transfer and fluid flow model can also predict temperature field, velocity field, pressure field of the melt pool, clad height, and melt pool geometry. The measurement of these quantities is not presented here since this paper focus on the prediction of dilution.

6. Conclusions

A self-consistent laser deposition model is presented, which simulates heat transfer, fluid flow, melt pool geometry during the laser deposition process. The SOLA-VOF[25] method is adopted to track the evolution of the melt pool free surface (liquid/vapor interface). The continuum model [15, 16] is applied to derive the mass, momentum and energy conversation equations, which are valid for solid and liquid. The movement of solid/liquid interfaces are also simulated using the continuum model[15, 16]. In this study, processes associated with the melt pool free surface, including free surface evolution, convection, evaporation, surface tension, heating of powder particles, powder flow velocities, and powder concentration distribution have been modeled.

The numerical model is used to predict diode laser-induced dilution in Ti-6Al-4V that was in agreement with those measured by SEM. The sources of the errors between the simulated and measured dilution have been analyzed. It is expected that a three dimensional model with finer mesh will improve the accuracy of prediction in dilution.

Acknowledgments

This research was supported by the National Science Foundation Grant Number DMI-9871185, the grant from the U.S. Air Force Research Laboratory contract # FA8650-04-C-5704, and UMR Intelligent Systems Center. Their support is greatly appreciated.

References

1. R.R. Unocic and J.N. DuPont, “Composition Control in the Direct Laser-Deposition Process,” Metallurgical and Materials Transactions B. Vol. 34B, no. 8, pp. 439-, 2003.
2. H. Gedda, A. Kaplan, and J. Powell, “Melt-Solid Interactions in Laser Cladding and Laser Casting,” Metallurgical and Materials Transactions B. Vol. 36B, no.10, pp.683-, 2005.
3. T. C. Lei, J. H. Ouyang, Y. T. Pei, and Y. Zhou, “Microstructure and Sliding Wear Properties of Laser Clad TiN reinforced Composite Coating,” Surface Engineering, vol. 12 no. 1 pp.55-60, 1996.
4. A. F. H. Kaplan and G. Groboth, “Process Analysis of Laser BeamCladding,” Journal of Manufacturing Science and Engineering (Transactions of the ASME) (USA). Vol. 123, no. 4, pp. 609-614. Nov. 2001
5. K. G. Watkins, “Achieving the Potential of Direct Fabrication with Lasers,” Proc 3rd International Conference on Laser Asssisted Net Shaping (LANE 2001) Erlangen, 28-31 August, 2001 pp 25-38 Meisenbach- Verlag Bamberg.
6. M. L. Griffith, et. al., Materials and Design, vol. 20, pp. 107-113, 1999.
7. W. Hofmeister, et. Al., JOM, vol. 51, no.7, 1999.
8. A. Vasinonta, J. Beuth, and M. Griffith, Proceedings of the Solid Freeform Fabrication Symposium, Austin, TX, pp. 383-391, 1999.
9. C. A. Brice, K. I. Schwendner, D. W. Mahaffey, E. H. Moor, and H. L. Fraser, Proceedings of the Solid Freeform Fabrication Symposium, Austin, TX, pp. 369-374, 1999.
10. J. Brooks, C. Robino, T. Headley, S. Goods, and M. Griffith, Proceedings of the Solid Freeform Fabrication Symposium, Austin, TX, pp. 375-382,1999.
11. Blake, A.G. and Eboo, G.M.,“State of the Art Laser Hardfacing Using Dynamic Powder Feed Technology,”Conference on the Laser vs. the Electron Beam in Welding, Cutting and Surface Treatment, Reno, Nevada, pp. 196-214, 1985.
13. Kennedy, E; Byrne, G; Collins, D N, “A review of the use of high power diode lasers in surface hardening,” Journal of Materials Processing Technology. Vol. 155-156, pp. 1855-1860. 30 Nov. 2004.
14. Ezugwu, E. O. and Wang, Z. M. Titanium alloys and their machinability-a review, J. Mater. Processing Technol., 1997, 68(3), 262-274.
15. W. Bennon and F. Incropera, International Journal of Heat and Mass Transfer, vol. 30, pp. 2161-70, 1987.
16. W. Bennon and F. Incropera, International Journal of Heat and Mass Transfer , vol. 30, pp. 2171-87, 1987.
17. C. R. Swaminathan, and V. R. Voller, “A General Enthalpy Method for Modeling Solidification Processes,” Metallurgical Transactions B (USA). Vol. 23B, no. 5, pp. 651-664. Oct. 1992
18. C. Prakash and V. Voller, Numerical Heat Transfer, vol.15B, pp171-89, 1989
19. S. Asai and I. Muchi, Trans. Iron Steel Inst. Jpn., vol. 18, pp. 90-98, 1978.
20. Todd E. Sparks and Zhiqiang Fan, measurement of laser absporption coefficient of several alloys for diode laser, unpublished report, 2006.
21. A. Frenk, M. Vandyoussefi, J Wagniere, A. Zryd, and W. Kurz: Metall. Mater. Trans. B,

1997, vol. 28B, pp. 501-07.
22. M. Choi, R. Greif and M. Salcudean, Numerical Heat Transfer, vol. 11, pp477-489, 1987.
23. L. Han, F.W. Liou, and K.M. Phatk, Metallurgical and Materials Transactions B. Vol. 35B, no. 6, pp. 1139-1150B. Dec. 2004.
24. Andrew J. Pinkerton and Lin Li, Journal of Manufacturing Science and Engineering, vol. 126, pp. 33-41, February 2004.
25. J.M. Jouvard, D.F. Grevey, F. Lemoine, and A.B. Vannes: J. Laser Appl., vol. 9, pp. 43-50, 1997.
26. B. D. Nichols, C.W. Hirt, R. S. Hotchkiss, “SOLA-VOF: A solution algorithm for transient fluid flow with multiple free boundaries,” LA-8355, Los Alamos National Laboratory.
27. Henry Hu and Stavros A Argyropoulos, “Mathematical modeling of solidification and melting: a review,” Modelling Simula. Mater. Sci. Eng. 4, pp.371-396, 1996.
28. Heng Pan and Frank Liou, Journal of Materials Processing Technology. Vol. 168, no. 2, pp. 230-244. 30 Sept. 2005.
29. S.M. Kelly, “Thermal and Microstructure Modeling of Metal Deposition Processes with Application to Ti-6Al-4V”, Ph.D. thesis, Virginia Polytechnic Institute and State University, 2004.
30. K. C. Mills, “Recommended values of thermophysical properties for selected commercial alloys,” Woodhead, Cambridge, 2002.
31. Tobias Lips and Bent Fritsche, "A COMPARISON OF COMMONLY USED RE-ENTRY ANALYSIS TOOLS", 55th International Astronautical Congress 2004 - Vancouver, Canada IAC-04-IAA.5.12.2.09, P.9, SCARAB model.
32. A. F. H. Kaplan and G. Groboth, “Process Analysis of Laser BeamCladding,” Journal of Manufacturing Science and Engineering (Transactions of the ASME) (USA). Vol. 123, no. 4, pp. 609-614. Nov. 2001.
33. F. Liou, J. Choi, R. Landers, V. Janardhan, S. Balakrishnan, and S. Agarwal: Proc. 12th Annual Solid Freeform Fabrication Symp., Austin, TX, Aug. 6–8, 2001, pp. 138-45.
34. 36. M. Boddu, S. Musti, R. Landers, S. Agarwal, and F. Liou: Proc. 12th Annual Solid Freeform Fabrication Symp., Austin, TX, Aug. 6–8, 2001, pp. 452-59.